STUDY OF ENERGY TRANSFER BETWEEN LANTHANIDE IONS IN ZIRCONIA NANOCRYSTALS

A THESIS

submitted to

Indian Institute of Science Education and Research Pune

in partial fulfilment of the requirements for the BS-MS Dual Degree Programme

by

ANJU B MODAN

(20201029)

Indian Institute of Science Education and Research Pune

Dr. Homi Bhabha Road,

Pashan, Pune 411008, INDIA

May 2025

Supervisor : Prof. Dr. Jonathan De Roo

भारतीय विज्ञान शिक्षा एवं अनुसंधान संस्थान पुणे
Indian Institute of Science Education and Research Pune
(Estb. By MoE, Govt. of India)

CERTIFICATE

This is to certify that this dissertation entitled **Study of Energy Transfer between Lanthanide Ions in Zirconia Nanocrystals** towards the partial fulfilment of the BS-MS dual degree programme at the Indian Institute of Science Education and Research, Pune represents study/work carried out by **Anju B Modan** at University of Basel, Switzerland, under the supervision of **Prof. Dr. Jonathan De Roo**, Associate Professor, Department of Chemistry, during the academic year 2024 - 2025.

Anju B Modan

Prof. Dr. Jonathan De Roo

Prof. Pramod Pillai

Committee:

Prof. Dr. Jonathan De Roo

Prof. Pramod Pillai

DECLARATION

I hereby declare that the matter embodied in the report entitled "Study of Energy Transfer between Lanthanide Ions in Zirconia Nanocrystals" are the results of the work carried out by me at the University of Basel, Switzerland, under the supervision of Prof. Dr. Jonathan De Roo, Department of Chemistry, and the same has not been submitted elsewhere for any other degree. Wherever others contribute, every effort is made to indicate this clearly, with due reference to the literature and acknowledgement of collaborative research and discussions.

Anju B Modan

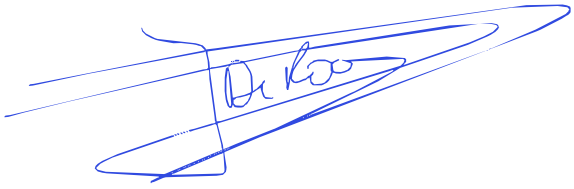

Prof. Dr. Jonathan De Roo

Contents

ACKNOWLEDGEMENT

First and foremost, I would like to thank my supervisor, Prof. Dr. Jonathan De Roo, for inviting me to his lab to carry out the project. I thank him for the discussions and for giving pointers when required. I enjoyed my scientific talks with him, which made me even more fascinated by this field. I also thank Prof. Pramod Pillai for his exceptional guidance and support as an expert.

I thank my mentor, Mr Nico Reichholf, who took time out of his busy schedule to guide me throughout the project. I'm incredibly grateful to him for getting me interested in the many peaks we sought out in the PL measurements. I also thank all the De Roo group members, Liza, Evelina, Harry, Carlotta, Ian, Ajmal, Jikson, David, and Jibin, for making me feel at home despite being away from India. They were incredibly supportive and made me feel included in all group activities. All the group parties which ended with board games will always be dear to me.

I want to thank my parents, who made this visit possible. The emotional support from them and my sister was much needed being away from home. I would also like to thank my friends who supported me in my times of need. Yatish was a constant support and companion throughout the thesis. Jason, Krishna, Kashika, Pooja, Joseph and Anuj were there for me when I needed someone to talk to. Their company helped me in ways I cannot express. I enjoyed my time in Europe with Manav, Ananthu, Rifa, Devapriyan and Bhageerath, with whom I could explore and make everlasting memories.

This project was more than just an academic endeavour; it was a journey filled with learning, friendships, challenges, and unforgettable experiences. I am genuinely grateful to every person who was a part of it.

Anju B Modan

This thesis is dedicated to all the experience I gained throughout the commencement of this thesis. All of it helped me become the person I currently am. Thank you Basel!

LIST OF ABBREVIATIONS

NPs	Nanoparticles
NCs	Nanocrystals
ZrO_2	Zirconium dioxide
Tb^{3+}	Terbium (III)
Eu^{3+}	Europium (III)
ICP-OES	Inductively Coupled Plasma Optical Emission Spectroscopy
TEM	Transmission Electron Microscopy
TRES	Time-resolved Emission Spectra

LIST OF FIGURES

LIST OF TABLES

ABSTRACT

This project mainly aims to study the energy transfer between the lanthanide ions, Terbium and Europium, doped in zirconia nanocrystals. Europium (III) is a vital lanthanide ion as it has narrow and strong emissions in the red region of the visible range. This helps it be easily detected using fluorescence spectroscopy. Eu^{3+} ions find application in various optical fields, bioimaging, and environment sensors and are also used in up- and down-conversion of light. They are also excellent indicators of their local environment, as reflected in the emission spectra. However, they only weakly absorb blue light and emit in a narrow range. As they cannot give a full spectrum emission, their scope of application is limited.

Terbium (III) has an intense green emission and absorbs in the blue range of the visible spectrum. Using a sensitiser (Tb^{3+}) that can absorb blue light and transfer this energy to the activator (Eu^{3+}) by a non-radiative resonant energy transfer can help increase its scope of usage.

Zirconia (ZrO_2) acts as an excellent host for these ions, allowing energy transfer studies to be conducted in the same system. ZrO_2 is biocompatible; hence, lanthanide-doped zirconia nanocrystals can be used in bio-medical fields.

Chapter 1

Introduction

Nanoparticles are materials in the size range of 1 to 100 nm. They find applications in the field of sensing [1], catalysis [2], bio-medical [3] and nano electronics [4]. NPs have a high surface-to-volume ratio, making them different from their macroscopic counterpart. As the size decreases considerably, a shift in thermodynamic equilibrium properties, like melting point, is observed. There are different classifications of NPs; metallic [5] metal oxides [6], polymeric [7], carbon based [8], quantum dots [9] etc. This thesis focuses on metal oxide nanoparticles, specifically zirconia nanoparticles.

There are two approaches to synthesising a nanoparticle: *top-down* and *bottom-up*. The former involves breaking down a macroscopic material to give a nanomaterial. The high-energy ball milling process is one example of macroscopic materials being ground into smaller nanoscale materials [10]. A major disadvantage comes in synthesising particles below 10 nm resolution. The *bottom-up* approach takes care of this problem. It allows the growth of the material in the nanoscale range. However, this approach restricts the synthesis of particles to sizes smaller than 10 nm [11]. Synthesising good-quality particles at an industrial scale also poses a challenge to this synthesis procedure.

Metal oxide nanoparticles include group 4 transition metal oxides like titanium dioxide (TiO_2), zirconium dioxide (ZrO_2) and hafnium dioxide (HfO_2). Zirconium and hafnium oxides possess similar properties. They exist in cubic, tetragonal and monoclinic crystal phases based on temperature. The monoclinic phase of zirconia is stable at room temperature, changes to tetragonal at 1170°C and after 2370°C is stabilised in the cubic phase [12]. Selecting the appropriate synthesis route can help stabilise the tetragonal phase of ZrO_2 at lower temperatures [12],[13]. The properties of ZrO_2 include high thermal and chemical stability [14], large band gap [15], which makes them an excellent host material. Moreover, this material shows a high refractive index, allowing them to be used as optical materials[16]. The phonon energy of ZrO_2 is low, which decreases the luminescence thermal quenching compared to other materials [17]. These crystals have been used as catalysts [18], in fuel cells [19], gate dielectrics [20].

One disadvantage is that zirconia is not luminescent. But, luminescence can be in-

duced by introducing optically active lanthanide ions like europium, terbium, erbium, and thulium [21],[22], amongst others. Lanthanide doping has been well studied in fluoride hosts like $NaYF_4$ and $NaGdF_4$. These systems are used for both up-conversion as well as down-conversion of light [23],[24]. Multi-shelled nanoparticles allow for lanthanides to be spatially separated, and an energy cascade process can allow for a single wavelength excitation into full spectrum emissions [24]. These lanthanide-doped fluoride systems have found applications in the biomedical field, bioimaging and biosensing [25], targeted drug delivery [26]. However, despite being widely popular in the biomedical field, there is a significant concern regarding the dissolution of $NaYF_4$ NPs in aqueous media, which will result in leaching of the toxic fluoride and lanthanide ions [27].

Due to the chemical stability of the oxide hosts, luminescent ZrO_2 can be used as the safer alternative to fluoride NPs in the biomedical field. They have been used as a time-resolved fluorescence resonance energy transfer (FRET) bioprobe to detect avidin. Using Tb^{3+} ion, specific targeting of cancerous cells was also done [28].

In this project, the synthesis of zirconia nanocrystals and the subsequent shelling is introduced to study the optical properties of the nanoparticles. Lanthanide-doped cores were synthesised using a surfactant-free solvothermal process involving benzyl alcohol and a surfactant-assisted nonhydrolytic sol-gel reaction between zirconium (IV) isoproxide and zirconium (IV) chloride at 340°C. The former synthesis route is termed autoclave synthesis. As the second synthesis is performed in the presence of tri-*n*-octylphosphine oxide (TOPO), this synthesis route is termed TOPO synthesis. The nucleation and growth mechanism of ZrO_2 nanocrystals from TOPO synthesis have been previously elucidated, and it suggests that before reaching the crystalline phase, soon after the decomposition of the precursors, amorphous nanoparticles are formed [29]. The cores nanoparticles from both syntheses behaved differently when comparing their optical properties. When shelling was introduced around the doped cores, surface quenching effects were significantly reduced. This could have been due to interaction with the surface ligands or other defects in the crystal lattice. Improved quantum yields and longer fluorescence lifetimes are indicative of the enhanced quality of the core/shell systems [14], [30].

The lanthanide ions that were mainly examined in this thesis are Eu^{3+} and Tb^{3+}. They emit light in the visible region. Eu^{3+} is a common dopant to achieve red emission. It has a ground state of $^7F_0$, and the most common excited states are ^5D_J (J = 0-4). The most intense peak corresponds to the transition from $^5D_0 \rightarrow {}^7F_2$ ($\sim$ 606 nm) [31]. Eu^{3+} ions can be used as a probe for their local environment, such as the surface of the nanocrystal and site symmetry of the system. Such changes are reflected in their fluorescence spectra [14]. The $^5D_0 \rightarrow {}^7F_2$ are the hypersensitive transitions which strongly depend on their environment. This transition is forbidden if the europium ion is present at a site with an inversion centre, according to Judd-Ofelt theory [32]. This suggests that if Eu^{3+} is present in a high-symmetry site with an inversion centre, the $^5D_0 \rightarrow {}^7F_2$

transition becomes weak. But if the symmetry is lowered, that is if the inversion centre is lost, the transitions become stronger. These differences are observed in the synthesised Eu-doped cores and Eu-doped core/shell explored in this thesis, shedding light on the symmetry of the synthesised nanoparticles.

Tb^{3+} emits light in the green region. $^7F_6$ is the ground state, and emission is observed from the excited states $^5D_3/^5D_4$. The most intense peak is due to the $^5D_4 \rightarrow {}^7F_5$ transition ($\sim$ 543 nm) [31]. However, doping these ions in the ZrO_2 matrix leads to the formation of crystal defects. The ionic radius of Zr^{4+} is approximately 84 pm [33], while the ionic radii of Eu^{3+} and Tb^{3+} are 107 pm [34] and 92.3 pm [35], respectively. Because of the introduction of larger ions into the system, the crystal lattice gets distorted. Oxygen vacancies are created for every two lanthanide (III) ions, replacing the Zr(IV) cation, which can then be a potential site for luminescence quenching. Other non-radiative relaxation pathways involve interaction with ligands on the surface and phonon coupling reactions.

Recent emphasis has been put on the development of Eu^{3+} doped phosphors for LED applications, but since Eu^{3+} is a weak absorber in the blue and near-ultraviolet region, its application is limited [36]. Using a sensitiser ion, which is optically active and can absorb the desired wavelength of the light and transfer this absorbed light to an emitter ion, can help Eu^{3+} be used as phosphors for white LEDs [37]. Previously used sensitisers to enhance the usage of blue light were Eu^{2+}, Ce^{3+}, Bi^{3+}, Pb^{2+} [36], [38], [39], [40]. However, the choice of the sensitiser ions also depends on the host material being used. This issue is addressed by using Tb^{3+} as the sensitiser ion. Eu^{3+} can be sensitised by Tb^{3+} by the process of Förster resonance energy transfer (FRET) [37]. Tb^{3+} absorbs light in the blue region, which Eu^{3+} is not excited by. Furthermore, both ions have previously been shown to be compatible with our host material ZrO_2 [28], [41].

Different architectures were synthesised to study the energy transfer between the lanthanide ions. This involves having the ions in separate cores, co-doping the ions in a core, and spatially separating the lanthanide ions in a core/shell structure. A study was also carried out by having an additional shell of ZrO_2 on particles that show energy transfer. Finally, a new core/shell/shell architecture was synthesised, wherein the inert shell is introduced between two active layers in order to study the extent to which FRET can occur.

Chapter 2

Methodology

2.1 Materials

Zirconium (IV) propoxide, 70% in propanol and benzyl alcohol ($\geq$ 99%) were purchased from Sigma-Aldrich. Europium (III) acetate hydrate (99.9%-Eu) and terbium (III) acetate hydrate (99.9%-Tb) were purchased from Strem Chemicals and used without purification. Benzyl alcohol (Sigma-Aldrich, $\geq$ 99%) was dried over $MgSO_4$ and filtered and, after air-free distillation into a Strauss flask and subsequently stored inside the glovebox. $ZrCl_4$ (99.9%) and $ZrBr_4$ (98%) were purchased from Strem Chemicals. $Zr(O^iPr)_4{\cdot}^iPrOH$ (99.9%), $EuBr_2$ (99.9%), acetone (99.8%), and toluene (99.5%) were purchased from Sigma Aldrich and used without further purification. TOPO (99%) was purchased from Strem Chemicals and recrystallised according to Owen *et al.*[42]. $ZrCl_4{\cdot}2THF$ was synthesised according to Manzer *et al* [43].

2.2 Synthesis of lanthanide-doped core nanoparticles

Autoclave synthesis

ZrO_2 NPs doped with europium or terbium were synthesised from lanthanide acetates, zirconium propoxide, and benzyl alcohol following a slightly modified previously reported synthesis [28],

$$0.9\,\mathrm{Zr(OPr)4} + 0.1\,\mathrm{Ln(OAc)3} + 40\,\mathrm{BnOH} \xrightarrow[\mathrm{[Zr]=0.20\,mol/L}]{72\,\mathrm{h},\,230\,^\circ\mathrm{C}} \mathrm{ZrO2:\ Ln\ NCs} + \text{by-products} \tag{2.1}$$

The autoclaves were prepared and assembled in a nitrogen-filled glovebox ($O_2 < 2$ ppm, $H_2O < 1$ ppm). The precursors were weighed in a glass vial; $Zr(OPr)_4$ in 70% PrOH (1.6 mL, 3.6 mmol), benzyl alcohol (16.6 mL, 160 mmol) and lanthanide acetate (0.4

mmol) The lanthanides (Ln) used were europium and terbium acetates. To dissolve the precursors in benzyl alcohol, the precursors were heated to 60°C for an hour. This dissolved solution was transferred to a Teflon liner, and the autoclave was assembled. These were transferred to a muffle furnace. The temperature was increased to 230°C at a rate of 3°C/min and was left for 72 hours.

After the completion of the reaction, the suspension was transferred to a centrifuge tube. It was washed twice with 30 mL ether by sonicating for 5 minutes and centrifugation at 8000 rpm for 3 minutes to collect the product. To make the particles perfectly soluble in non-polar solvents, the particles were functionalised with a ligand: 300 μL of 99% pure oleic acid for Eu-doped cores and 750 mg of decanoic acid for Tb-doped cores, with 3 mL toluene were added to the particles, which were then sonicated until the solution was clear (about 30 minutes). Then, the particles were washed from the excess ligands by precipitating with 10 mL acetone, centrifugation (8000 rpm for 3 minutes), and dissolved in 3 mL toluene again by sonicating for 15 minutes. This washing procedure was performed three times, leading to perfectly purified particles. The particles were dried entirely to determine the yield (by measuring TGA) and then redissolved in cyclohexane. Cyclohexane has an absorption range below 200 nm. This becomes significant when studying the fluorescence of the synthesised nanoparticles, making it a useful solvent. The yield obtained for Eu-doped particles is 71.1%, whereas for Tb-doped particles, the yield is 72.2%.

TOPO synthesis

By slightly modifying the reported procedure [12], doped core particles were synthesised from $ZrCl_4{\cdot}2THF$, $Zr(O^iPr)_4{\cdot}^iPrOH$ and $LnCl_3$ in TOPO. The required apparatus was dried at 150°C (three-neck flask, condenser, cold finger, clamps) and was loaded into the glovebox overnight.

$$1\,ZrCl_4(THF)_2 + 1\,Zr(O^iPr)_4{\cdot}^iPrOH + 0.1\,LnCl_3 \xrightarrow[\text{TOPO}]{2\,\text{h},\,340\,^\circ\text{C}} ZrO_2:\ \text{Ln NCs} \tag{2.2}$$

$ZrCl_4{\cdot}2THF$ was used instead of $ZrCl_4$ as the tetrahydrofuran complex is better soluble in TOPO [44].

To synthesise nanocrystals of smaller sizes for europium-doped particles, the precursors were changed as follows:

$$1\,ZrBr_4 + 1\,Zr(O^iPr)_4{\cdot}^iPrOH + 0.1\,EuCl_3 \xrightarrow[\text{TOPO}]{2\,\text{h},\,340\,^\circ\text{C}} ZrO_2:\ \text{Eu NCs} \tag{2.3}$$

$$1\,ZrCl_4(THF)_2 + 1\,Zr(O^iPr)_4{\cdot}^iPrOH + 0.1\,EuBr_2 \xrightarrow[\text{TOPO}]{2\,\text{h},\,340\,^\circ\text{C}} ZrO_2:\ \text{Eu NCs} \tag{2.4}$$

All precursors were added in layers in a three-neck flask; $ZrCl_4{\cdot}2THF$ (0.377 g, 1 mmol),

$Zr(O^iPr)_4.^iPrOH$ (0.387 g, 1 mmol), $LnCl_3$ (0.1 mmol) and recrystallised TOPO (10 g, 26 mmol). The setup was completed with a condenser with a tap, septa, and a cold finger. This was brought out of the glovebox and connected to the Schlenk line with a vacuum of 10 mTorr and argon. The hose was flushed three times using a vacuum and filled with argon. The setup was then filled with argon, and a constant flow was allowed. The reaction mixture was heated to 340°C and run for 2 hours. After completion of the reaction, the mixture was left to cool to 100°C. 1.5 mL toluene was added to the flask to stop the solidification of TOPO.

The resulting particles were collected and washed by transferring the resulting product into a centrifuge tube, then precipitation with 20 mL acetone, centrifugation (8000 rpm for 3 minutes) and redissolving the particles with 1 mL toluene. The washing procedure was repeated two more times. Since TOPO and its decomposition products (di-*n*-octylphosphonate and *P*, *P*′-(di-octyl) pyrophosphonate) are ligands attached to the nanoparticle surface [45], it does not need to be functionalised with ligands to be soluble in non-polar solvents. After the purification step, the particles were completely dried and redissolved in cyclohexane. The yield obtained for Eu-doped particles is 72.8%, whereas for Tb-doped particles, the yield is 57.8%.

2.3 Synthesis of core/shell nanoparticles

Core nanoparticles from previous syntheses (Eu-doped and Tb-doped particles from autoclave synthesis (Equation 2.1)) were used for shelling.

$$1\,ZrCl_4(THF)_2 + 1\,Zr(O^iPr)_4{\cdot}^iPrOH + x\,ZrO_2{:}\,Ln\,NCs \xrightarrow[\substack{\text{TOPO}\\ [Zr]_{complexes} = 0.20\ \text{mol/kg}\\ [\text{cores}] = 70\text{ - }90\ \mu\text{mol/kg}\\ [A_{tot}] = 1400\text{ - }2300\ m^2/kg}]{2h,\ 340°C} ZrO_2{:}Ln/\,ZrO_2\,NCs \tag{2.5}$$

The core particles were directly dried into an oven-dried three-neck flask. The flask was closed with septa and loaded into the glovebox. The remaining precursors were added in layers in the three-neck flask: TOPO, $ZrCl_4{\cdot}2THF$ and $Zr(O^iPr)_4{\cdot}^iPrOH$. The precursors were layered such that they would not be in contact with each other. Hence, TOPO was added in between the layers of the zirconia precursors. The amounts of precursors to core amount were varied as required. Changing the ratios can lead to different thicknesses of the shell. As the amount of cores used in the synthesis is increased, the amount of precursors left to shell each core particle decreases, thus leading to the formation of thinner shells.

The setup was completed with a condenser with a tap, septa, and a cold finger. This was brought out of the glovebox and connected to the Schlenk line with a vacuum of

10 mTorr and argon. The hose was flushed three times using a vacuum and filled with argon. The setup was then filled with argon, and a constant flow was allowed. The reaction mixture was heated to 340°C and run for 2 hours. After the completion of the reaction, the mixture was left to cool to 100°C. 1.5 mL toluene was added to the flask to stop the solidification of TOPO.

The resulting particles were collected and washed by transferring the resulting product into a centrifuge tube, then precipitation with 20 mL acetone, centrifugation (8000 rpm for 3 minutes) and redissolving the particles with 1 mL toluene. The washing procedure was repeated twice, and the particles were dried completely and redissolved in cyclohexane.

2.4 Synthesis of nanoparticles for energy transfer

Core synthesis

The doped cores used for this experiment were synthesised using the autoclave method discussed in Equation 2.1. Both Eu-doped and Tb-doped cores are synthesised with a nominal doping of 10%.
For codoped cores, nominal doping percentages of 10 and 5 were maintained for terbium and europium, respectively,

$$0.85\,\mathrm{Zr(OPr)_4} + 0.05\,\mathrm{Eu(OAc)_3} + 0.1\,\mathrm{Tb(OAc)_3} + 40\,\mathrm{BnOH} \xrightarrow[\text{[Zr] = 0.20 mol/L}]{\text{72h, 230°C}} \mathrm{ZrO_2}:\ \mathrm{Eu/Tb\ NCs} + \text{by-products} \tag{2.6}$$

Core/shell synthesis

For the core/shell synthesis, Tb-doped (10%) cores from the autoclaves were used as the seed particles. Using a TOPO synthesis, Eu-doped shell was introduced;

$$1\,\mathrm{ZrCl_4(THF)_2} + 1\,\mathrm{Zr(O^{\mathit{i}}Pr)_4{\cdot}^{\mathit{i}}PrOH} + 0.1\,\mathrm{EuCl_3} + x\,\mathrm{ZrO_2}\text{: Tb NCs} \xrightarrow[\substack{\text{TOPO}\\ [\mathrm{Zr}]_{complexes} = 0.20\ \text{mol/kg}\\ [\text{cores}] = 92\ \mu\text{mol/kg}\\ [\mathrm{A}_{tot}] = 2000\ \mathrm{m^2/kg}}]{\text{2h, 340°C}} \mathrm{ZrO_2}\text{:Tb/ }\mathrm{ZrO_2}\text{:Eu NCs} \tag{2.7}$$

Core/shell/shell synthesis

For the core/shell/shell synthesis, Tb-doped cores from autoclaves were used as the initial seed particles (Equation 2.1). A shell of ZrO_2 was grown on top of this in a TOPO synthesis according to Equation 2.5. To ensure that we get core/shells of uniform thickness, selective precipitation of the reaction mixture was done. For this, the product, after the first shelling process, was purified three times with toluene and acetone. After

this, the particles were dispersed in excess cyclohexane ($\sim$ 5 mL). To this, acetone was added dropwise until the whole solution turned turbid. The turbid solution was then centrifuged for 1 minute at 8000 rpm. The precipitate was redissolved in cyclohexane, whereas the supernatant was collected, and to this, acetone was again added dropwise. Multiple fractions were collected by this method, and each fraction was characterised by TEM to find the thickness of ZrO_2 around the Tb-doped core. The desired core/shells were then shelled again to introduce Eu ions into the nanoparticle.

$$1\,\mathrm{ZrCl_4(THF)_2} + 1\,\mathrm{Zr(O^{\mathit{i}}Pr)_4{\cdot}^{\mathit{i}}PrOH} + 0.1\,\mathrm{EuCl_3} + x\,\mathrm{ZrO_2{:}Tb/\,ZrO_2\,NCs} \xrightarrow[\substack{\text{TOPO}\\ [\mathrm{Zr}]_{complexes} = 0.20\ \text{mol/kg}\\ [\text{cores}] = 15\text{ - }35\ \mu\text{mol/kg}\\ [\mathrm{A}_{tot}] = 945\text{ - }1000\ \mathrm{m^2/kg}}]{\text{2h, 340°C}} \mathrm{ZrO_2{:}Tb/\,ZrO_2/\,ZrO_2{:}Eu\,NCs} \tag{2.8}$$

2.5 Characterisation techniques

Photoluminescence (PL) Spectroscopy

All fluorescence measurements were done on the FS5 Spectrofluorometer by Edinburgh Instruments. For all indirect measurements (where the host matrix is excited), solutions of particles with an absorbance of approximately 0.1 at excitation wavelength are used. For direct measurements (where the lanthanide ions are excited), a particle concentration of 100 mg/mL is used throughout unless specified otherwise.

Lifetime measurements are done on a photo spectrometer with a microsecond flash-lamp at 25 Hz. Time-resolved emission spectral (TRES) measurements are done with the same at a lamp frequency of 80 Hz.

Transmission Electron Microscopic (TEM) Analysis

TEM imaging was performed on the JEOL JEM-F200 cFEG instrument. The nanoparticles were diluted to a concentration of 2.5 mg/mL in cyclohexane and then drop-casted onto a carbon mesh for measurement. The size analysis was done using ImageJ software, where more than 100 particles were mapped.

Inductively Coupled Plasma Optical Emission Spectroscopy (ICP-OES)

ICP-OES measurement was done by Mikrolabor Pascher. The dissolution is a proprietary procedure and is thus not disclosed by the company.

Nuclear Magnetic Resonance (NMR) Analysis

NMR analysis was done on a 500 MHz Brucker UltraShield spectrometer. After purifying the nanoparticles, ∼15 mg of dried particles are dissolved in 500 μL of chloroform-d ($CDCl_3$) or benzene-d_6 (C_6D_6) and measured.

Thermogravimetric Analysis (TGA)

TGA analysis was performed on a TGA5500 instrument. The samples were heated to 800°C at a ramping rate of 5°C/min.

Chapter 3

Results and Discussion

3.1 Lanthanide doped core nanoparticles

Comparing the two synthesis routes

Eu-doped and Tb-doped particles were synthesised using the autoclaves (Equation 2.1) and by the TOPO synthesis (Equation 2.2)

To determine the composition of the nanocrystals, ICP-OES was performed on Eu-doped and Tb-doped cores synthesised from autoclaves and in TOPO (Table 3.1). The results showed that the incorporation of the lanthanide ions was higher when particles were synthesised using autoclaves. Eu^{3+} is incorporated with 90% efficiency, whereas Tb only had a 50% incorporation in the particles synthesised in autoclaves. Also, Tb^{3+} is incorporated significantly less than Eu^{3+} in TOPO synthesis.

Synthesis route	Dopants	Nominal doping	Actual doping
Autoclaves	$Eu(OAc)_3$	10%	9%
	$Tb(OAc)_3$	10%	5%
TOPO	$EuCl_3$	10%	1.5%
	$TbCl_3$	10%	$< 0.1\%$

Table 3.1: Nominal vs actual doping percentages of lanthanides in NPs

The surface chemistry of the synthesised lanthanide-doped core particles from the autoclave was analysed using ^{1}H NMR spectroscopy. A broad resonance is observed for the bound ligands due to their heterogeneous environment and their attachment to a larger particle [46]. When a lanthanide is present in the system, an additional paramagnetic broadening is observed due to the presence of unpaired electrons in the lanthanides. This difference is observed when comparing the NMR spectra of non-doped zirconia and Eu-doped and Tb-doped zirconia nanocrystals. Also, the broadening of the ^{1}H NMR peaks is a preliminary indicator of the successful doping of lanthanides. TGA analysis performed on the doped core nanoparticles synthesised in the autoclaves showed that 75.5% of the measured yield was from the inorganic content of the nanoparticle. Hence, the percentage

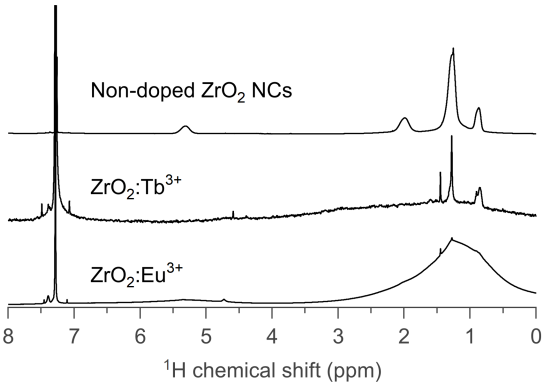

Figure 3.1: ^{1}H NMR spectra for non-doped ZrO_2 and Eu-doped and Tb-doped core nanoparticles (synthesised in autoclaves) in $CDCl_3$.

yields for the synthesised doped core particles were calculated.

The optical characterisation of these particles was done using photoluminescence spectroscopy. In the excitation spectra of Eu-doped NPs, particles from the autoclave show two peaks (250 nm and 280 nm). But the peak around 280 nm gets suppressed in the particles synthesised in TOPO (Figure 3.2a). As for the Tb-doped particles, the peak at 235 nm for the autoclave particles is shifted to 230 nm for particles from TOPO synthesis (Figure 3.2d). The intensity of the peak at 280 nm increases for the TOPO-synthesised particles. On measuring the emission of the Eu-doped particles, we see that there are differences in the appearance of peaks. The particles from TOPO synthesis have peaks at 606 nm and 614 nm, which do not overlap, as seen for the autoclave particles at 606 and 612 nm (Figure 3.2b). The reasoning for this is not well understood. A possible explanation could be due to the different crystallinity of the particles. When synthesised in TOPO, due to the higher reaction temperature used (340°), the crystallinity might be higher as compared to the ones synthesised in autoclaves (230°). Also, previous measurements using Scanning Transmission Electron Microscopy with Energy-Dispersive X-ray Spectroscopy (STEM-EDX) could not give conclusive results about the distribution of ions in the nanoparticles. In Tb-doped particles, the splitting of peaks at 543 nm is significant in the TOPO-synthesised particles (Figure 3.2d) again, which is not well understood.

Photoluminescence lifetimes Eu-doped particles show differences in the rate of decay. The lifetimes of Eu-doped cores are shown in Figure 3.2c, and the fits are summarised in Table 3.2. The peaks at position 614 nm have a shorter lifetime with respect to 606 nm, which was previously assigned to Eu ions located near the nanocrystal surface [14]. Interestingly, the 606 and 614 nm peaks show longer lifetimes for particles prepared in TOPO than those prepared in the autoclave. They also show a monoexponential decay when compared to the particles from the autoclave as these peaks do not overlap with each other. This can also be seen in the increased lifetimes in Table 3.2. A similar trend is observed for the Tb-doped particles (Figure 3.2f, Table 3.3). Particles from TOPO

synthesis have longer lifetimes compared to autoclave particles.

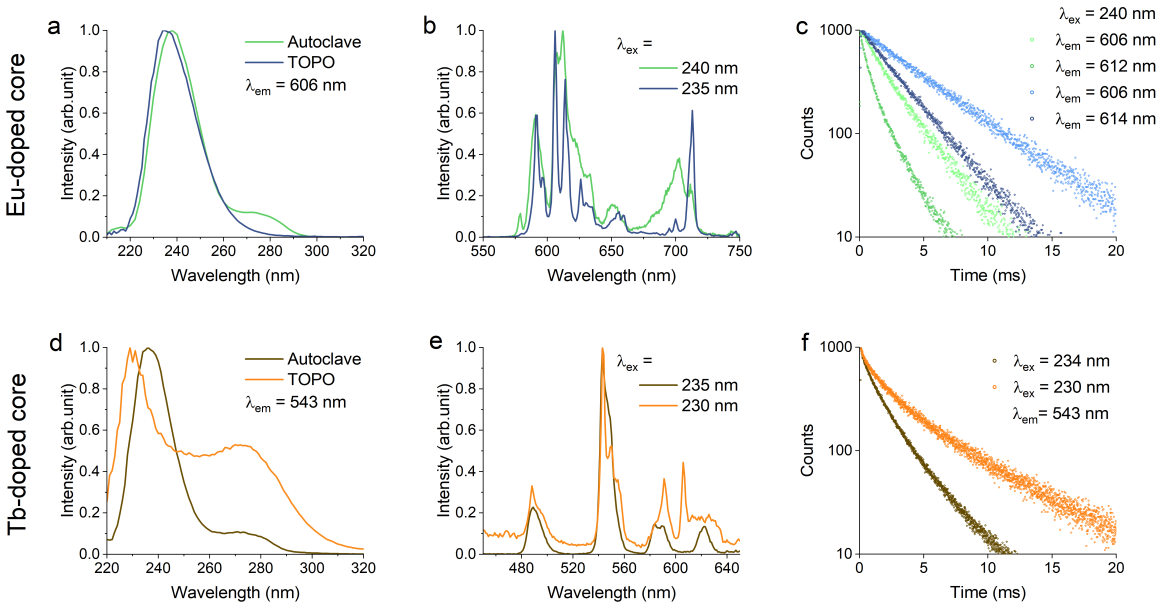

Figure 3.2: Differences in photoluminescence properties of 10% Eu-doped (a-c) and 10% Tb-doped (d-f) core nanoparticles prepared in autoclave and in TOPO. (a) Excitation spectra measured at 606 nm, (b) emission spectra measured excitation maxima and (c) lifetime decay after exciting at 240 nm and emission at 606 nm and 612/614 nm. (d) Excitation spectra measured at 543 nm, (e) emission spectra measured at excitation maxima and (f) lifetime decay after exciting at excitation maxima and emission at 543 nm.

Synthesis routes	Dopants	lifetime λ_{em} = 606 nm			lifetime λ_{em} = 612/614 nm			% yield of NCs
		τ_1 (ms)	τ_2 (ms)	ν_2 (%)	τ_1 (ms)	τ_2 (ms)	ν_2 (%)	
Autoclave	$Eu(OAc)_3$	1.1	2.9	90	0.6	2.1	59	71.1
TOPO	$EuCl_3$	1.8	5.0	97	1.4	3.0	93	72.8

Table 3.2: Lifetime decays calculated at emission peak 606 nm and 612/614 nm for particles synthesised in autoclaves and TOPO.

Synthesis routes	Dopants	lifetime λ_{em} = 543 nm			% yield of NCs
		τ_1 (ms)	τ_2 (ms)	ν_2 (%)	
Autoclave	$Tb(OAc)_3$	1.3	3.7	50	72.2
TOPO	$TbCl_3$	1.5	6.2	76	57.8

Table 3.3: Lifetime decays calculated at emission maxima 543 nm for particles synthesised in autoclaves and TOPO.

The photoluminescence decay was fitted to the formula:

$$N(t) = A_1.e^{-t/\tau_1} + A_2.e^{-t/\tau_2} \tag{3.1}$$

where N(t) was the measured decay as a function of time, A_1 and A_2 are scaling factors, τ_1 and τ_2 are the short and long lifetimes, respectively.
The relative amounts of the long component were calculated using:

$$\nu_2 = \frac{A_2.\tau_2}{A_1.\tau_1 + A_2.\tau_2} \tag{3.2}$$

Changing the size of europium doped particles

To identify how changing the precursors will affect the size of the doped particles, $ZrCl_4$·2THF was replaced by $ZrBr_4$ (Equation 2.3), or $EuCl_3$ by $EuBr_2$ (Equation 2.4) in the TOPO synthesis. In all three syntheses, a nominal doping of 10% (0.1 mmol of lanthanide source) of the lanthanide was maintained.

TEM analysis was performed to see if changing precursors changes the size of the nanoparticles from each synthesis. It shows that the size of Eu-doped NPs decreases on changing the precursors (Table 3.4). The particles grown using bromides grow faster and hence are smaller in size [44].

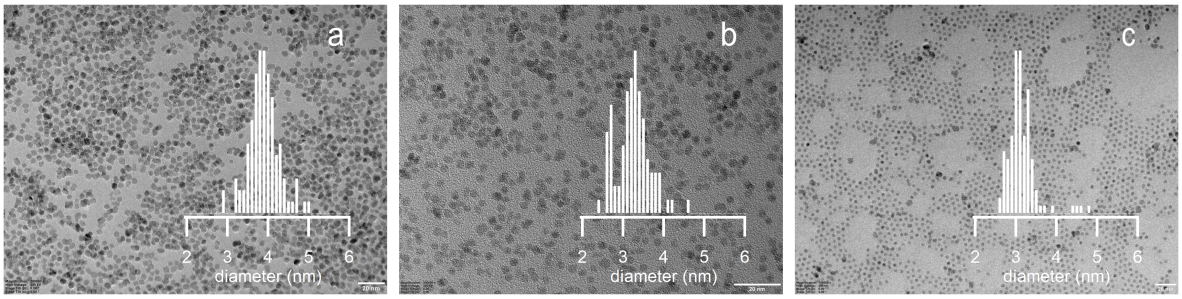

Figure 3.3: TEM images of Eu-doped cores by changing the precursors in TOPO synthesis. Precursors used in each are (a) $ZrCl_4$·2THF and $EuCl_3$, (b) $ZrCl_4$·2THF and $EuBr_2$ and (c) $ZrBr_4$ and $EuCl_3$.

Precursors used	sizes (nm)	% yield of NCs
$ZrCl_4$·2THF and $EuCl_3$	3.9 ± 0.4	72.8
$ZrCl_4$·2THF and $EuBr_2$	3.3 ± 0.4	48.1
$ZrBr_4$ and $EuCl_3$	3.2 ± 0.4	48.2

Table 3.4: Sizes of different Eu-doped cores from TEM imaging and their respective percentage yields.

These particles were also characterised using PL spectroscopy, and we found a few differences in their photoluminescence properties. The absorbance for all three solutions was kept constant. The excitation spectra are almost similar for the particles. The only difference is seen in the particles synthesised from $ZrBr_4$. The peak is narrower in this case (Figure 3.4a), and the noise-to-signal ratio is lower for these particles. This could be due to the low incorporation of europium ions in the matrix.

On exciting the NPs at the respective excitation maxima, we observe some changes in their emission peaks. The particles synthesised using $ZrCl_4$·2THF and $EuBr_2$ behave similarly to those synthesised using both chloride precursors. However, for the particles from $ZrBr_4$ and $EuCl_3$, the peak at 614 nm is more pronounced than the one at 606 nm. The photoluminescence lifetime decays of these particles are similar to the ones we saw above for the Eu-doped cores synthesised in TOPO (Figure 3.2c); they are monoexponential and longer. Particles synthesised using the bromides ($EuBr_2$ and $ZrBr_4$) have longer lifetimes, whereas chloride particles have a shorter lifetime. The particles synthesised using bromides are smaller leading to more ions being near the surface of the particles. But the lifetimes measured give an opposite trend, which is not well understood yet.

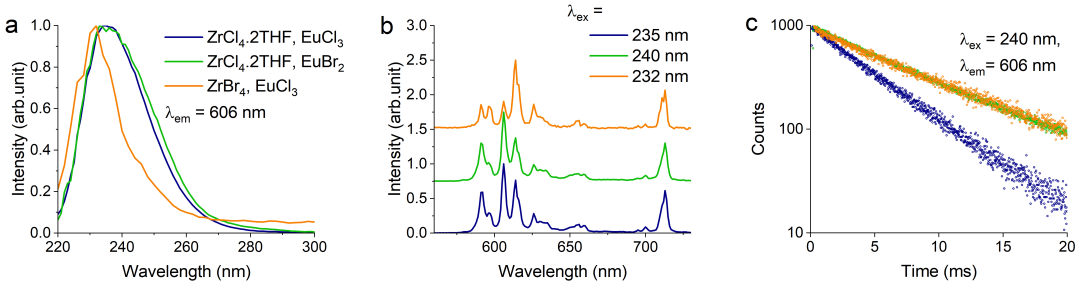

Figure 3.4: Differences in photoluminescence properties of 10% Eu-doped core nanoparticles prepared in TOPO by changing the precursors. (a) Excitation spectra measured at 606 nm, (b) emission spectra measured at excitation maxima and (c) lifetime decay after exciting at 240 nm and emission at 606 nm .

Not many differences are observed in the optical properties of the Eu-doped particles synthesised by changing the precursors. Hence, due to the higher cost of the bromide precursors and as previous literature focuses majorly on the chloride precursors, for the rest of the thesis, we utilise $ZrCl_4$·2THF and $EuCl_3$ for further synthesis.

3.2 Comparing core/shell to core nanoparticles

Core/shell was synthesised as described in Equation 2.5. After the particles are purified, they were characterised using NMR spectroscopy to study the surface chemistry of the synthesised nanoparticles. The purified particles were dissolved in 500 μL of benzene-d_6. C_6D_6 was used as the solvent as $CDCl_3$ strips off some of the TOPO from the surface, and hence in the ^{31}P NMR, free TOPO peaks appear (48 ppm) [45]. The ^{1}H NMR spectrum shows a broad peak, confirming the bound nature of the ligands (3.5a). The ^{31}P NMR shows a broad resonance around 73 ppm, 58 ppm and 21 ppm, which were assigned to tri-*n*-octylphosphine oxide (TOPO), di-*n*-octylphosphine oxide (DOPA) and *P,P'*-(di-*n*-octyl) pyrophosphonate (PPA) (3.5b) [45].

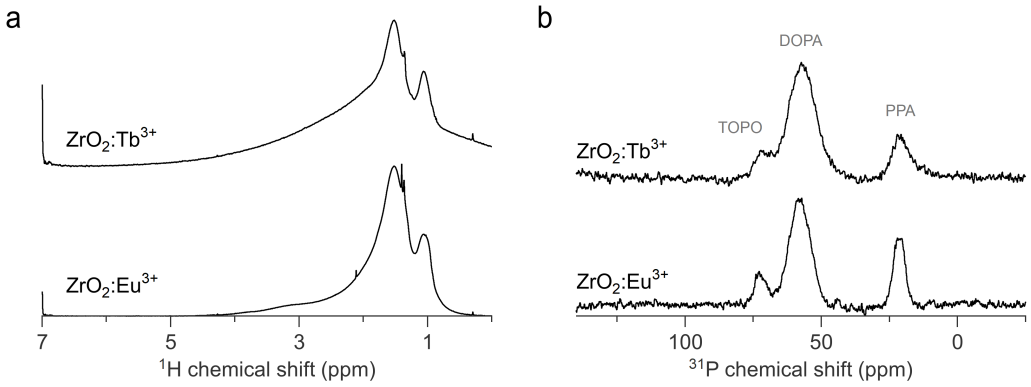

Figure 3.5: (a)^{1}H and (b) ^{31}P NMR spectra for Eu-doped and Tb-doped core/shell nanoparticles in C_6D_6.

TEM imaging was done to measure the size of the shell around the doped cores. Eu-doped core/shell grew to an average diameter of 4.8 nm (core size was 3.2 nm) (Figure A.1) whereas, Tb-doped core/shell seems to have grown from 3.5 to 4.5 nm in size (Figure A.2). The shell size can be altered by varying the amount of doped core NPs during the synthesis.

The core/shell particles were then characterised by PL spectroscopy to observe the differences in the optical properties of the doped cores from when a shell was introduced on these core NPs. On shelling Eu-doped cores, the peak at 280 nm disappears in the excitation spectra (Figure 3.6a). However, in the Tb-doped core/shell, there is a shift in the major peak from 240 nm to 280 nm (Figure 3.6d).

Upon shelling, the emission peak at 612 nm disappeared in the Eu-doped core/shell (Figure 3.6b). This peak was previously assigned to the ions present towards the surface [14]. The remaining peaks also become narrower. This is indicative of the change in the local environment around the europium ion. The change in the emission peaks from that of the cores could be an indicator of the loss of symmetry on the addition of the shell, intensifying the $^{5}D_0 \rightarrow {}^{7}F_2$ transition. In the Tb-doped core/shell, the emission peaks become more defined (Figure 3.6d). The shell also brings in a difference in the lifetime of the excited state of ions. The decay becomes monoexponential when the cores are shelled (Figures 3.6c and 3.6f). The fast decay (τ_1) is suppressed (Tables A.1 and A.2), indicating the minimal energy loss by interaction with ligands and other surface ligands.

The doped core/shell nanoparticles also show optical properties similar to that of the doped core nanoparticles synthesised in TOPO, indicating a similar crystallinity of the core/shell particles and the doped core nanoparticles synthesised in TOPO.

The core/shell architecture was further modified to synthesise core/shell/shell NPs to study the energy transfer between the lanthanide ions Tb and Eu (intraparticle energy transfer), where the ions were spatially separated within the system.

3.2. Comparing core/shell to core nanoparticles

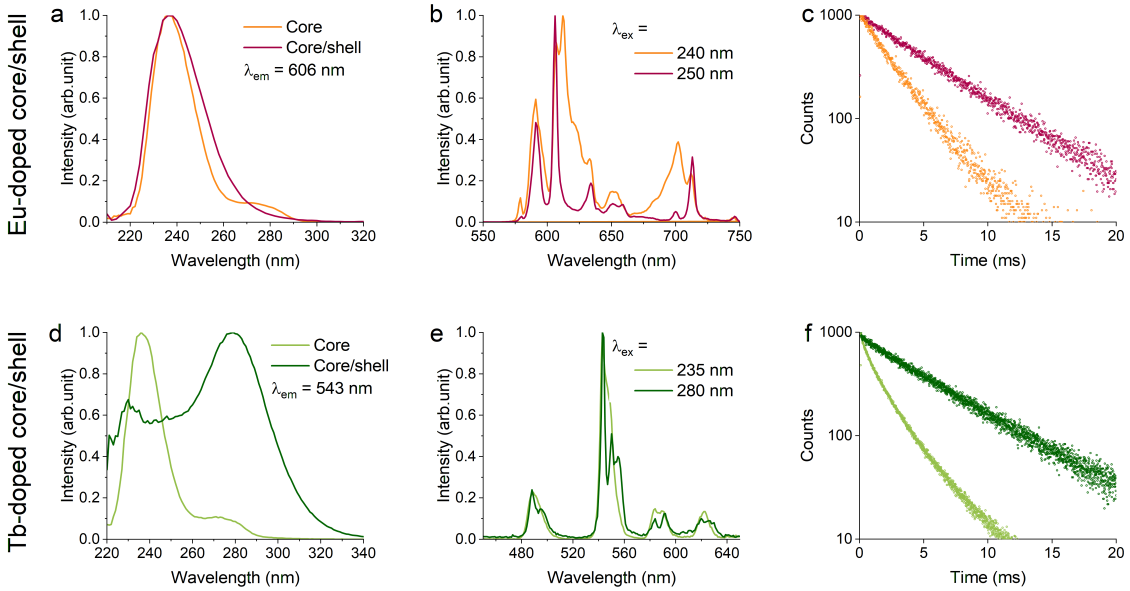

Figure 3.6: Differences in photoluminescence properties of 10% Eu-doped (a-c) and 10% Tb-doped (d-f) core/shell nanoparticles. (a) Excitation spectra measured at 606 nm, (b) emission spectra measured at excitation maxima and (c) lifetime decay after exciting at 240 nm and emission at 606 nm. (d) Excitation spectra measured at 543 nm, (e) emission spectra measured at excitation maxima and (f) lifetime decay after exciting at excitation maxima and emission at 543 nm.

3.3 Energy transfer between lanthanide ions

The efficiency of energy transfer was calculated using the following equation,

$$E = 1 - \frac{\tau_{DA}}{\tau_D} \tag{3.3}$$

where τ_{DA} represents the lifetime of the donor when both the donor (Tb^{3+}) and acceptor (Eu^{3+}) ions are present, and τ_D denotes the lifetime of the donor when just the donor ion is present in the nanoparticle. The efficiency of core particles (a mixture of lanthanide-doped cores and codoped core particles) was calculated with respect to Tb-doped cores. In contrast, for core/shell and core/shell/shell nanoparticles, which have both Tb^{3+} and Eu^{3+} present within the same nanoparticles, calculations were done with respect to the Tb-doped core with a ZrO_2 shell.

The individual lifetimes were calculated as an average from the decay over the Tb^{3+} emission, using the following equation:

$$\langle \tau \rangle = \frac{\sum^i a_i {\tau_i}^2}{\sum^i a_i \tau_i} \tag{3.4}$$

To investigate the energy transfer between the lanthanide ions terbium and europium,

terbium ions were directly excited. This ensured that the excitation of the lanthanide ions, both Tb^{3+} and Eu^{3+}, were not influenced by charge transfer from the host matrix. For this, we first determined the optimal excitation wavelength required to excite the synthesised nanoparticles described below. For this purpose, a 100 mg/mL solution was prepared for both doped cores. High concentrations facilitate tracking of the energy transfer process by directly exciting the lanthanide ions. Also, the f-f transitions in the lanthanide ions are forbidden, making their emissions weak according to the Laporte selection rules. Thus, a higher concentration also ensures the detection of these weak emissions.

The excitation spectra reveal that Tb^{3+} is efficiently excited at 486 nm (Figure 3.7) without overlapping with the excitation spectrum of Eu^{3+}. Previously, interparticle Förster resonance energy transfer (IFRET) was studied between Tb^{3+} and Eu^{3+} by using the blue excitation (485 nm) of terbium ion [37]. Therefore, 486 nm was selected as the excitation wavelength to investigate the extent of energy transfer between the lanthanide ions throughout this study. In this section, the concentration of nanoparticles was kept at 100 mg/mL. Also, the energy transfer study was conducted using a time-resolved emission spectral measurement as a steady-state emission gives rise to a spectrum with a weak signal-to-noise ratio, which involves a broad band which is due to the emission from the host matrix zirconia (Figure B.3).

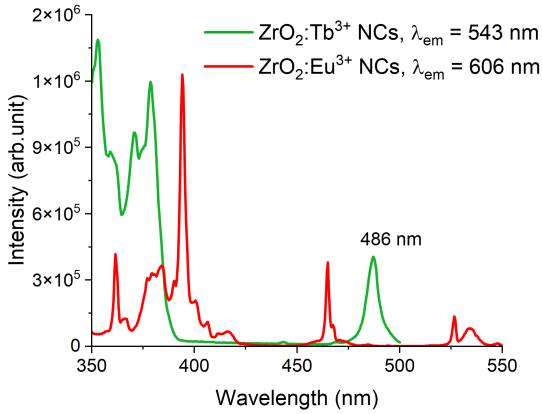

Figure 3.7: Photoluminescence measurement of Tb-doped and Eu-doped cores (at concentration 100 mg/mL) to determine the excitation maximum of terbium ion.

To study the energy transfer between the ions, we first tried to discern between inter- and intra-particle energy transfers. As a first step, the extent of energy transfer was measured by mixing Tb-doped cores and Eu-doped cores and then exciting the system at 486 nm. A time-resolved emission spectral (TRES) measurement was taken at 486 nm over the range of 520 to 730 nm. The decay was then integrated over the $^5D_4 \rightarrow {}^7F_5$ emission of Tb^{3+} (from 535-570 nm) to determine the efficiency of energy transfer. A detailed explanation of this measurement is given in Section B.1.

3.3. Energy transfer between lanthanide ions

The energy transfer efficiency when both the doped-core nanoparticles are mixed is less than 3%. As inter-particle energy transfer is not very prominent, we investigate intra-particle energy transfer, wherein both the ions are present in a single nanoparticle, either co-doped in the core or spatially separated in a core/shell or core/shell/shell architecture.

On measuring the energy transfer efficiency in a codoped system (5% Eu + 10% Tb nominal doping), the extent of energy transfer is calculated to be 59.8%. This could be attributed to the proximity of the ions to each other in the nanoparticle. To investigate the importance of shelling in the energy transfer process, a layer of inert ZrO_2 was shelled on the codoped nanoparticles. In these particles, the efficiency increased to 64.7% (Figure 3.8). The increase in transfer efficiency could be because terbium ions are well protected from undergoing non-radiative decay and, hence, are able to transfer energy to the europium ions more effectively. Also, emission peaks of Eu^{3+} increased in intensity and became sharper when a shell was introduced (Figure B.4). This is in corroboration with what was shown in Section 3.2.

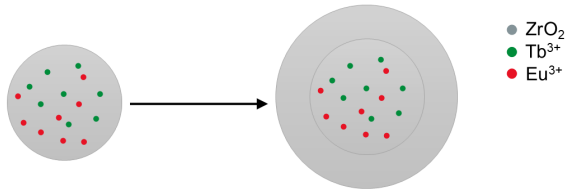

Figure 3.8: A schematic showing the codoped core (both terbium and europium ions) nanoparticles and these nanoparticles on shelling with a layer of ZrO_2.

Next, nanoparticles were synthesised where the lanthanide ions were spatially separated in different layers. To do so, we shelled a layer of Eu-doped zirconia on top of Tb-doped core nanoparticles synthesised in the autoclaves. The resultant particles are characterised by TRES measurement by directly exciting Tb^{3+} at 486 nm. Energy transfer is observed in this system as well and is calculated to be about 58.3%. A layer of inert ZrO_2 is then shelled on top of these particles to synthesise a core/shell/shell structure. Here, we see an increase in the efficiency of energy transfer to about 81.4% (Figure 3.9). The increase in energy transfer, in this case, is not well understood because we expect the non-radiative decay pathways to be reduced when we introduce a layer of inert zirconia causing both τ_{DA} as well as τ_D to be large values. Hence, the increase in energy transfer cannot be explained by this phenomena indicating other factors to be governing this process.

Finally, we try to distance the lanthanide ions in a single nanoparticle. This study was conducted to understand if the process of energy transfer would occur when an inert layer was introduced. For this, we first shell a layer of inert ZrO_2 around Tb-doped core particles from the autoclave. To ensure that we have particles with uniform shell thickness, we segregate the Tb-doped core/shell using the process of selective precipitation

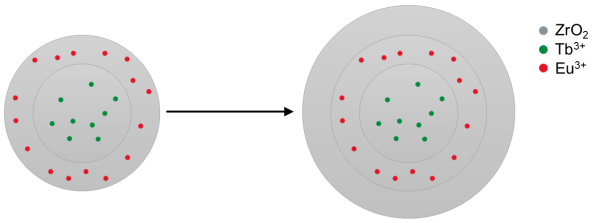

Figure 3.9: A schematic showing the core/shell nanoparticles which have a Tb-doped core and a layer of ZrO_2 shell that is doped with europium. A layer of ZrO_2 is introduced on these core/shell nanoparticles.

discussed in Section 2.4. TEM images of these core/shells were taken to ensure monodispersity in their size (Figure B.5). Three fractions were taken for this experiment with a shell thickness (d_{shell}) of 0.5 nm, 0.6 nm and 0.8 nm. These core/shells were then shelled again to introduce Eu^{3+} in the nanoparticle. The particles are structured as shown in Figure 3.10. Characterising the synthesised particles using TEM showed the presence of secondary nucleations along with the core/shell/shell nanoparticles (Figure B.6).

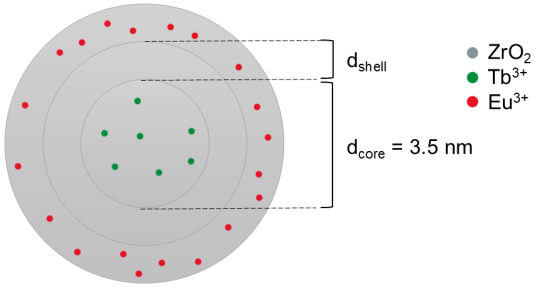

Figure 3.10: Synthesised core/shell/shell nanoparticle with an inert layer of ZrO_2 separating the lanthanide ions. The thickness of the inner shell (d_{shell}) is varied to study the extent of energy transfer.

The efficiency of energy transfer in core/shell/shell was also calculated after performing a TRES scan at 486 nm. We saw that for the particles with the thinnest inner shell (0.5 nm), the efficiency was 62.5%. When the inner shell was increased to 0.6 nm, the efficiency decreased to 47.9%. The decrease in energy transfer could be because, as the distance between the donor and the acceptor ions increases, the probability of the process of energy transfer occurring reduces, hence reducing the transfer efficiency. However, for a shell thickness of 0.8 nm, the efficiency unexpectedly increased to 84.8%. This could be because the shelling process is not uniform throughout, the thickness of the shell could be thinner in some places on the surface of the Tb-doped core particles. Also, the particles are represented as perfect spheres, but in reality, the particles have a more tetrahedral-like shape. As a result, when a second shell with Eu-doping is introduced, some Eu^{3+} would be located closer to the Tb^{3+} ions, leading to the energy transfer process to occur more efficiently. However, this observation deviates from the expected trend of decreasing

energy transfer efficiency with increasing inert shell thickness.

A summary of the change in the efficiency of energy transfer on introducing a layer of ZrO_2 between the lanthanide ions is shown in Figure 3.11.

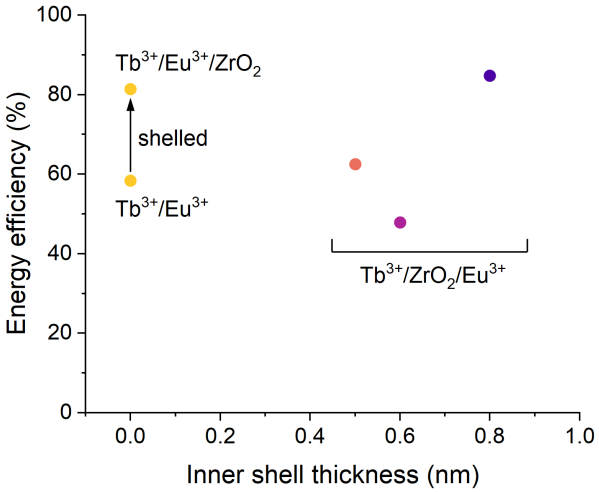

Figure 3.11: Change in energy transfer efficiency on increasing the thickness of the inert shell introduced between the lanthanide ions.

Chapter 4

Conclusion

This thesis mainly focuses on studying the energy transfer between the lanthanide ions terbium and europium. To do so, we first synthesised our doped-core particles by two synthesis routes. The choice of synthesis pathway seems to influence the chemistry of particles. On performing elemental analysis on the samples (ICP-OES), it was confirmed that lanthanide incorporation is higher in particles synthesised in autoclaves. TOPO synthesis shows minimal incorporation with respect to the nominal doping intended. Amongst the lanthanides, europium is more present in the system than terbium from both syntheses. A comparison between the doped particles shows some significant differences in their optical properties. In Eu-doped core particles, the excitation peak at 280 nm is suppressed in TOPO synthesis. The emission peaks are sharper and do not overlap (606 and 614 nm). Since we observe that the $^5D_0 \rightarrow {}^7F_2$ transition is strong, it indicates that the synthesised nanoparticles lack a centre of symmetry. The decay of TOPO particles is almost monoexponential compared to the particles from autoclave synthesis. This could indicate that the distribution of Eu^{3+} in the ZrO_2 matrix is different. They also have a significantly longer time of decay. Eu-doped nanoparticles of smaller sizes could be synthesised by changing the precursors used in the TOPO synthesis. In Tb-doped core particles, the particles from TOPO synthesis show an increase in the peak intensity at 280 nm. The emission peaks are also sharper than the peaks of particles from autoclave synthesis. The particles from TOPO show an increased lifetime. This again could elude to the differences in the distribution of Tb^{3+} in the ZrO_2 matrix.

A layer of ZrO_2 is introduced on the surface of these NCs to enhance the optical properties of the doped core particles. The growth of the shell is confirmed by TEM imaging. In Eu-doped particles, it is seen that the peak at 280 nm gets suppressed, and the emission peaks are more defined and narrow when compared to the core particles. The peak disappears at 612 nm as the Eu ions are located in the core, away from the surface. The lifetime decay of the excited state further confirms this. The decay becomes monoexponential which suggests the absence of decay occurring due to interaction with surface ligands and other defects. In the Tb-doped core/shell, we observe a change in

intensities of the peak at 235 nm and 280 nm. The emission peaks also become more defined when compared with the respective doped core nanoparticles. The core/shell has a monoexponential decay, which has a longer lifetime with respect to the non-shelled particles. Both the doped core and doped core/shell nanoparticles are characterised using NMR spectroscopy to study their surface chemistry. A broad peak in the ^{1}H NMR confirmed the bound nature of the ligands to the surface.

The final part of this thesis focuses on studying the energy transfer between the ions terbium and europium. For this, multiple architectures involving both the ions were synthesised and analysed. Inter-particle energy transfer was significantly lower; hence, we tried incorporating both ions into a single particle to study the intra-particle energy transfer. First, we tried codoping both terbium and europium ions in the core nanoparticle and saw the occurrence of energy transfer. The transfer efficiency increased by introducing a layer of ZrO_2 around them due to the protective effect of the shell from surface defects and interactions with the surroundings. Next, we synthesised particles where the lanthanide ions were present in different layers. Core/shell and core/shell/shell architectures were utilised for this. When terbium and europium were present in two different layers, energy transfer could be observed to the extent of 58.3%. This increased when a layer of inert ZrO_2 was introduced. Finally, we tried synthesising particles where a layer of ZrO_2 separated the lanthanide ions. We could segregate fractions of different shell thicknesses (core/shell) for this using a process of selective precipitation. On introducing europium through a shelling process, we observed a decreasing trend in energy transfer for inner shell thickness of 0.5 and 0.6 nm. This could be explained by the increasing distance between the ions, limiting the energy transfer process from terbium to europium. However, for the particles with an inner shell thickness of 0.8 nm, the transfer efficiency increases dramatically to 81.4%. This cannot be explained by the earlier reasoning, suggesting a different mechanism governing this process, or a mistake in the synthesis. To confirm the trend in energy transfer efficiency with respect to the inner shell thickness (and to exclude outliers), the same experiment with a wider range in shell size and number of analysed particles needs to be done.

Bibliography

[1] Chao Wang and Chenxu Yu. "Detection of chemical pollutants in water using gold nanoparticles as sensors: a review." In: *Reviews in Analytical Chemistry* 32.1 (2013), pp. 1–14.

[2] Shana Shirin et al. "Accelerated Reduction of 4-Nitrophenol: Bridging Interaction Outplays Reducing Power in the Model Nanoparticle-Catalyzed Reaction." In: *The Journal of Physical Chemistry C* 124.35 (2020), pp. 19157–19165.

[3] Krishnendu Chatterjee et al. "Core/shell nanoparticles in biomedical applications." In: *Advances in colloid and interface science* 209 (2014), pp. 8–39.

[4] Melanie Homberger and Ulrich Simon. "On the application potential of gold nanoparticles in nanoelectronics and biomedicine." In: *Philosophical Transactions of the Royal Society A: Mathematical, Physical and Engineering Sciences* 368.1915 (2010), pp. 1405–1453.

[5] Prasad Govindrao Jamkhande et al. "Metal nanoparticles synthesis: An overview on methods of preparation, advantages and disadvantages, and applications." In: *Journal of drug delivery science and technology* 53 (2019), p. 101174.

[6] Hengzhong Zhang and Jillian F Banfield. "Understanding polymorphic phase transformation behavior during growth of nanocrystalline aggregates: insights from TiO2." In: *The Journal of Physical Chemistry B* 104.15 (2000), pp. 3481–3487.

[7] Christine Vauthier and Kawthar Bouchemal. "Methods for the preparation and manufacture of polymeric nanoparticles." In: *Pharmaceutical research* 26 (2009), pp. 1025–1058.

[8] Valentin N Popov. "Carbon nanotubes: properties and application." In: *Materials Science and Engineering: R: Reports* 43.3 (2004), pp. 61–102.

[9] Debasis Bera et al. "Quantum dots and their multimodal applications: a review." In: *Materials* 3.4 (2010), pp. 2260–2345.

[10] HJ Fecht et al. "Nanocrystalline metals prepared by high-energy ball milling." In: *Metallurgical Transactions A* 21 (1990), pp. 2333–2337.

[11] Namra Abid et al. “Synthesis of nanomaterials using various top-down and bottom-up approaches, influencing factors, advantages, and disadvantages: A review.” In: *Advances in Colloid and Interface Science* 300 (2022), p. 102597.

[12] Jin Joo et al. “Multigram scale synthesis and characterization of monodisperse tetragonal zirconia nanocrystals.” In: *Journal of the American Chemical Society* 125.21 (2003), pp. 6553–6557.

[13] Weizhen Li et al. “Facile synthesis of pure monoclinic and tetragonal zirconia nanoparticles and their phase effects on the behavior of supported molybdena catalysts for methanol-selective oxidation.” In: *Langmuir* 24.15 (2008), pp. 8358–8366.

[14] Carlotta Seno et al. “Epitaxial Core/Shell Nanocrystals of (Europium-Doped) Zirconia and Hafnia.” In: *Journal of the American Chemical Society* 146.30 (2024), pp. 20550–20555.

[15] AK Singh and Umesh T Nakate. “Microwave synthesis, characterization, and photoluminescence properties of nanocrystalline zirconia.” In: *The Scientific World Journal* 2014.1 (2014), p. 349457.

[16] Deunchan Lee, Hanjun Cho, and Ilsun Yoon. “Zirconia nanocomposites and their applications as transparent advanced optical materials with high refractive index.” In: *Bulletin of the Korean Chemical Society* 44.4 (2023), pp. 284–292.

[17] Krisjanis Smits et al. “Europium doped zirconia luminescence.” In: *Optical Materials* 32.8 (2010), pp. 827–831.

[18] James F Haw et al. “NMR and theoretical study of acidity probes on sulfated zirconia catalysts.” In: *Journal of the American Chemical Society* 122.50 (2000), pp. 12561–12570.

[19] Rudzani Sigwadi, Touhami Mokrani, and Mokhotjwa Dhlamini. “The synthesis, characterization and electrochemical study of zirconia oxide nanoparticles for fuel cell application.” In: *Physica B: Condensed Matter* 581 (2020), p. 411842.

[20] Glen D Wilk, Robert M Wallace, and JáM Anthony. “High-κ gate dielectrics: Current status and materials properties considerations.” In: *Journal of applied physics* 89.10 (2001), pp. 5243–5275.

[21] G Cabello et al. “Structure and optical characterization of photochemically prepared ZrO2 thin films doped with erbium and europium.” In: *Journal of Non-Crystalline Solids* 354.33 (2008), pp. 3919–3928.

[22] Hongwu Zhang et al. “Blue emission of ZrO2: Tm nanocrystals with different crystal structure under UV excitation.” In: *Journal of non-crystalline solids* 354.14 (2008), pp. 1559–1563.

[23] Shili Gai et al. “Recent progress in rare earth micro/nanocrystals: soft chemical synthesis, luminescent properties, and biomedical applications.” In: *Chemical reviews* 114.4 (2014), pp. 2343–2389.

[24] Dengfeng Peng et al. “Lanthanide-doped energy cascade nanoparticles: full spectrum emission by single wavelength excitation.” In: *Chemistry of Materials* 27.8 (2015), pp. 3115–3120.

[25] Jing Zhou, Zhuang Liu, and Fuyou Li. “Upconversion nanophosphors for small-animal imaging.” In: *Chemical Society Reviews* 41.3 (2012), pp. 1323–1349.

[26] Bo Yang et al. “Application of upconversion rare earth fluorescent nanoparticles in biomedical drug delivery system.” In: *Journal of Luminescence* 223 (2020), p. 117226.

[27] Elina Andresen et al. “Time-resolved luminescence spectroscopy for monitoring the stability and dissolution behaviour of upconverting nanocrystals with different surface coatings.” In: *Nanoscale* 12.23 (2020), pp. 12589–12601.

[28] Yongsheng Liu et al. “Amine-Functionalized Lanthanide-Doped Zirconia Nanoparticles: Optical Spectroscopy, Time-Resolved Fluorescence Resonance Energy Transfer Biodetection, and Targeted Imaging.” en. In: *Journal of the American Chemical Society* 134.36 (Sept. 2012), pp. 15083–15090. ISSN: 0002-7863, 1520-5126.

[29] Rohan Pokratath et al. “An amorphous phase precedes crystallization: Unraveling the colloidal synthesis of zirconium oxide nanocrystals.” In: *ACS nano* 17.9 (2023), pp. 8796–8806.

[30] Santosh K Gupta, RM Kadam, and PK Pujari. “Lanthanide spectroscopy in probing structure-property correlation in multi-site photoluminescent phosphors.” In: *Coordination Chemistry Reviews* 420 (2020), p. 213405.

[31] Bingzhu Zheng et al. “Rare-earth doping in nanostructured inorganic materials.” In: *Chemical Reviews* 122.6 (2022), pp. 5519–5603.

[32] Koen Binnemans. “Interpretation of europium (III) spectra.” In: *Coordination Chemistry Reviews* 295 (2015), pp. 1–45.

[33] Robert D Shannon. “Revised effective ionic radii and systematic studies of interatomic distances in halides and chalcogenides.” In: *Foundations of Crystallography* 32.5 (1976), pp. 751–767.

[34] Weijie Zhou et al. “Luminescence and cationic-size-driven site selection of Eu3+ and Ce3+ ions in Ca8Mg (SiO4) 4Cl2.” In: *Inorganic Chemistry* 57.23 (2018), pp. 14872–14881.

[35] Dinara R Khayrutdinova et al. “Effects of Tb3+ on properties of luminescent calcium sulfate cement.” In: *Open Ceramics* 18 (2024), p. 100587.

[36] Shuchao Xu et al. “Luminescence and energy transfer of Eu 2+/Tb 3+/Eu 3+ in LiBaBO 3 phosphors with tunable-color emission.” In: *Journal of Materials Chemistry C* 3.35 (2015), pp. 9112–9121.

[37] Marie Anne Van De Haar et al. “Eu3+ sensitization via nonradiative interparticle energy transfer using inorganic nanoparticles.” In: *The Journal of Physical Chemistry Letters* 11.3 (2020), pp. 689–695.

[38] AA Setlur. “Sensitizing Eu3+ with Ce3+ and Tb3+ to make narrow-line red phosphors for light emitting diodes.” In: *Electrochemical and Solid-State Letters* 15.6 (2012), J25.

[39] DV Krishna Reddy et al. “Enhancement of the red emission of Eu3+ by Bi3+ sensitizers in yttrium alumino bismuth borosilicate glasses.” In: *Journal of Molecular Structure* 1176 (2019), pp. 133–148.

[40] Vladimir Babin et al. “The role of Pb2+ as a sensitizer for Gd3+–Eu3+ down-conversion couple in fluorides.” In: *Radiation measurements* 38.4-6 (2004), pp. 767–770.

[41] Tsedev Ninjbadgar et al. “Synthesis of luminescent ZrO2: Eu3+ nanoparticles and their holographic sub-micrometer patterning in polymer composites.” In: *Advanced Functional Materials* 19.11 (2009), pp. 1819–1825.

[42] Jonathan S Owen et al. “Reaction chemistry and ligand exchange at cadmium-selenide nanocrystal surfaces.” In: *Journal of the American Chemical Society* 130.37 (2008), pp. 12279–12281.

[43] LE Manxzer et al. “31. Tetragtdrfuran Complexes of Selected Early Transition Metals.” In: *Inorganic Syntheses* 21 (1982), pp. 135–140.

[44] Rohan Pokratath et al. “Mechanistic insight into the precursor chemistry of zro2 and hfo2 nanocrystals; towards size-tunable syntheses.” In: *JACS Au* 2.4 (2022), pp. 827–838.

[45] Katrien De Keukeleere et al. “Stabilization of colloidal Ti, Zr, and Hf oxide nanocrystals by protonated tri-n-octylphosphine oxide (TOPO) and its decomposition products.” In: *Chemistry of Materials* 29.23 (2017), pp. 10233–10242.

[46] Jonathan De Roo et al. “Probing solvent–ligand interactions in colloidal nanocrystals by the NMR line broadening.” In: *Chemistry of Materials* 30.15 (2018), pp. 5485–5492.

Appendices

Appendix A

Lanthanide doped core and core/shell nanoparticles

A.1 TEM of Eu-doped cores and core/shell NCs

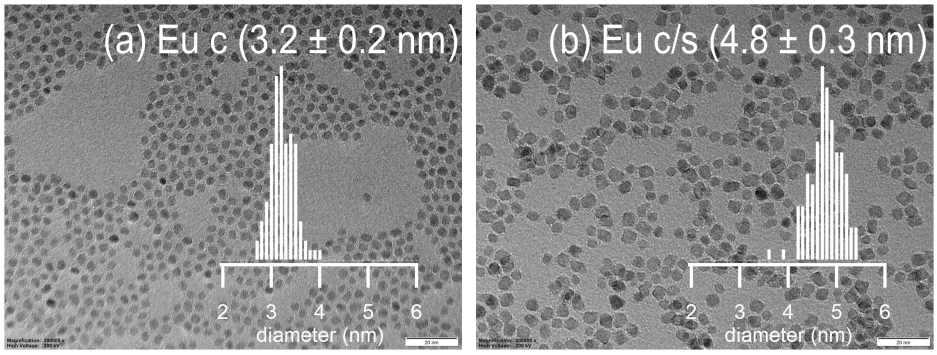

Figure A.1: (a) TEM images and histogram showing the size of 10% Eu-doped cores and (b) size of nanoparticles after shelling the Eu-doped cores with a layer of ZrO_2.

A.2 TEM of Tb-doped cores and core/shell NCs

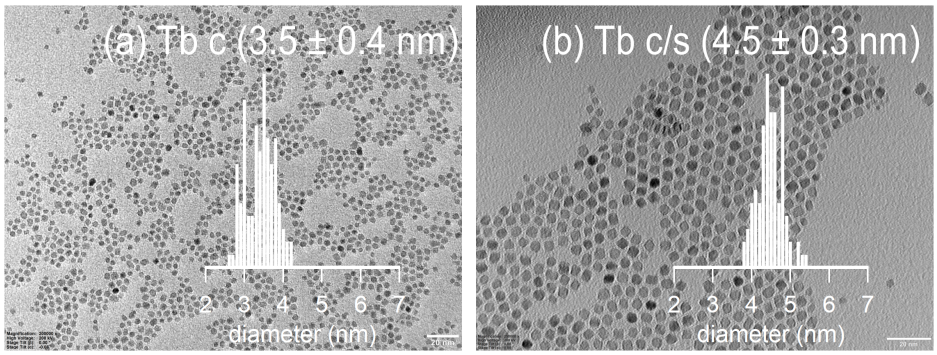

Figure A.2: (a) TEM images and histogram showing the sizes of 10% Tb-doped cores and (b) sizes of nanoparticles after shelling the Tb-doped cores with a layer of ZrO_2.

A.3 Photoluminescence lifetime decays

Dopants	λ_{ex} (nm)	lifetime λ_{em} = 606 nm τ_1 (ms)	τ_2 (ms)	ν_2 (%)
10% Eu	240	1.1	2.9	90
10% Eu c/s	240	-	5.4	100

Table A.1: Lifetime decays of Eu-doped cores and core/shell particles after exciting at 240 nm and emission at 606 nm.

Dopants	λ_{ex} (nm)	lifetime λ_{em} = 543 nm τ_1 (ms)	τ_2 (ms)	ν_2 (%)
10% Tb	240	1.2	4.1	74
10% Tb c/s	280	-	5.7	100

Table A.2: Lifetime decays of Tb-doped cores and core/shell particles after exciting at excitation maxima and emission at 543 nm.

Appendix B

Energy transfer between lanthanide ions

B.1 Time-resolved emission spectroscopy

Time-resolved emission spectroscopy (TRES) is used to study the evolution of fluorescence or phosphorescence emission over time. It allows us to study the lifetimes of excited states and energy transfer mechanisms. It involves capturing fluorescence emission spectra at different time delays after the excitation. The data from this measurement can be mapped as a 3D plot. An example of the result of a TRES measurement is shown in Figure B.1.

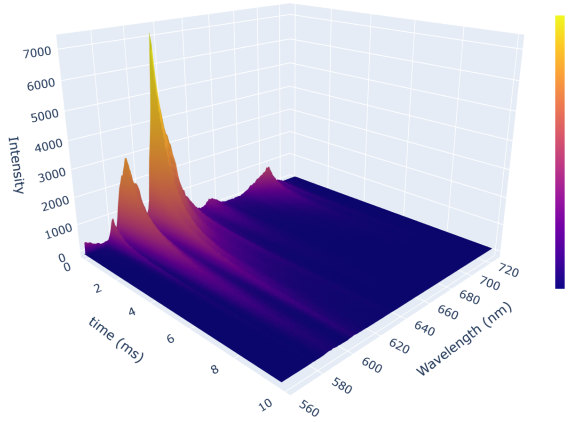

Figure B.1: TRES measurement of 10% Eu-doped core nanoparticles excited at 240 nm.

On integrating over an axis (time or wavelength), we obtain integrated 2D plots. When integrated over time, we obtain an integrated emission plot (Figure B.2a) that shows the evolution of emission over time (time-gated emission spectra). Whereas when integrated over wavelength, we obtain a decay curve (Figure B.2b) showing the overall decay profile over the entire wavelength. We can also integrate over a specific wavelength region, thus obtaining the decay of a specific transition (e.g. $^5D_0 \rightarrow {}^7F_2$). This has been done to fit τ_D and τ_{DA} in Section 3.3.

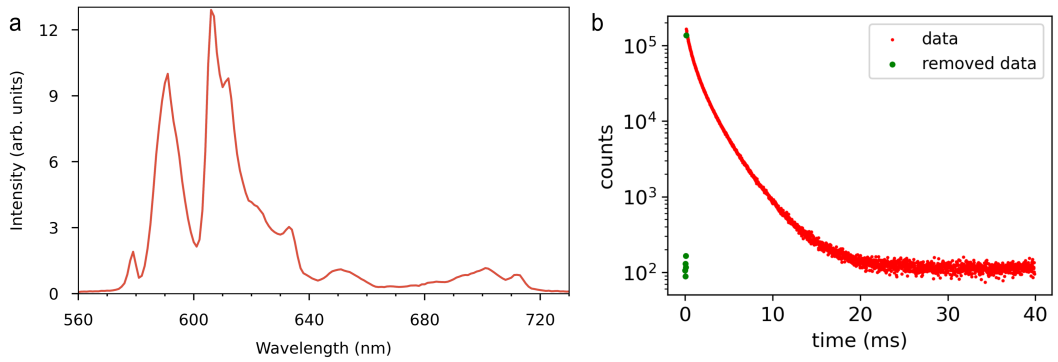

Figure B.2: Plots obtained after integrating over the time (a) and wavelength (b) axis.

In the integrated decay curve, we observe that we have at least two components since the decay is not monoexponential (which would result in a straight line in a semi-log plot). This curve can be then fit to the formula Equation 3.1. From this, the average lifetimes can be calculated which is then used to calculate the efficiency of energy transfer described in Equation 3.3

Time-gated emissions are useful when we are exciting the lanthanide ions in the matrix because, in steady-state emission, the signal-to-noise ratio is very poor, giving rise to a noisy emission spectrum. The noisy spectrum could be due to the low emission of the ions with respect to the host emission. Also, since the direct excitation of the ions is parity forbidden for lanthanides, the transition has a low probability of occurring, leading to the detection of a weak signal. Figure B.3 shows an example of a steady-state and a time-gated emission spectrum obtained on directly exciting terbium ions in a codoped core/shell nanoparticle containing both europium and terbium ions in the core.

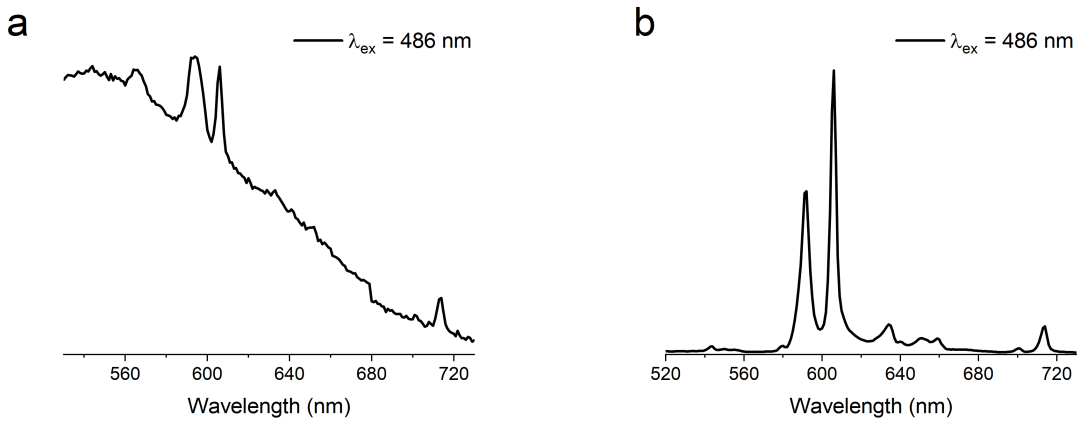

Figure B.3: Steady-state (a) and time-gated (b) emission spectrum of Tb and Eu codoped core/shell. The particles are excited at 486 nm to observe energy transfer between the lanthanide ions

B.2 Time gated emission to study energy transfer

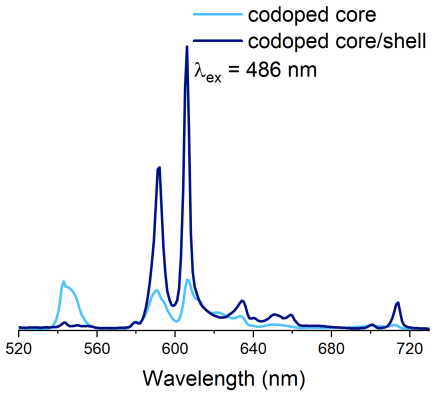

Figure B.4: Time gated emission spectra of codoped cores (with both Tb^{3+} and Eu^{3+} present together in the NP) and codoped core/shell particles measured at 486 nm.

B.3 Core/shell after selective precipitation

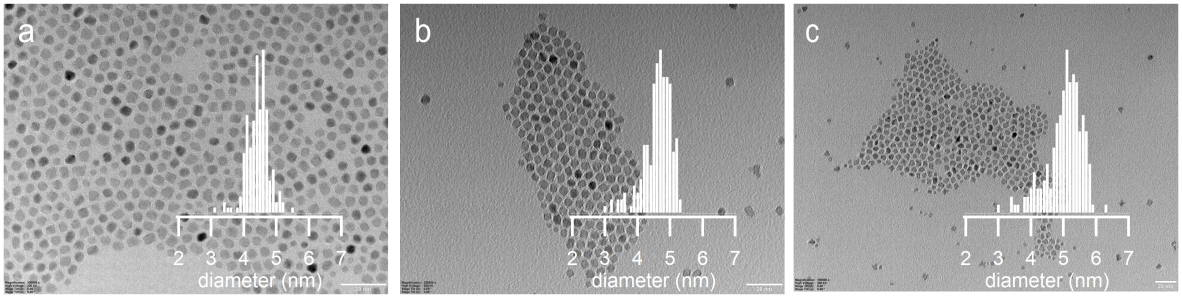

Figure B.5: TEM images of the core/shell (Tb-doped core/ZrO_2 shell) used to synthesise core/shell/shell. The thickness of the shell is (a) 0.5 nm, (b) 0.6 nm and (c) 0.8 nm.

B.4 TEM image of core/shell/shell

The histograms show two populations (Figure B.6). The size of each population was measured separately, and they were about 3.8 nm and 5.9 nm. The particles of size 5.9 nm are the core/shell/shell synthesised with an inner shell of ZrO_2 of thickness 0.6 nm (with a diameter of 4.6 nm). The particles of smaller size are secondary nucleations that were formed on the last step of the synthesis, used to introduce the second shell with Eu^{3+}. These particles might contain europium ions. However, since it was established that the efficiency of interparticle energy transfer was less than 3%, these particles were ignored when calculating the intraparticle energy transfer of the core/shell/shell.

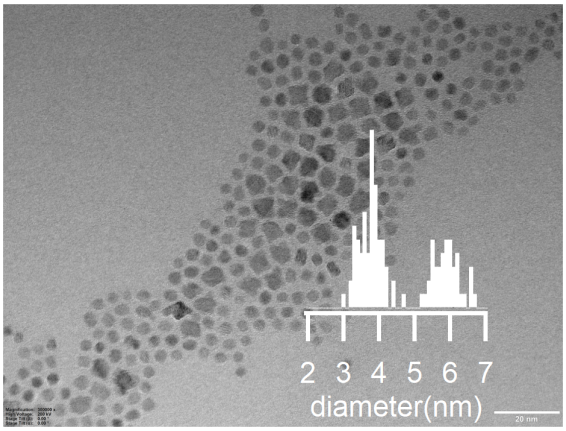

Figure B.6: TEM image showing the synthesised core/shell/shell along with the secondary nucleations.